Research Article

Journal of Environmental Nanotechnology

Influence of Pomegranate Peel-mediated Synthesis on the Physicochemical Characteristics and Photocatalytic Performance of CuO and TiO_2 Nanomaterials

V. P. Suresh Kumar[1*], Shailendra Kumar Yadav[2], S. Devarajsamy[3], J. Dhanasekaran[4], J. Kumaresan[5] and R. Girimurugan[6]

[1]Department of Mechanical Engineering, P.A. College of Engineering and Technology, Pollachi, TN, India
[2]Department of Mechanical Engineering, United College of Engineering and Research, Prayagraj, UP, India
[3]Department of Information Technology, Nandha College of Technology, Perundurai, TN, India
[4]Lecturer, Department of Mechanical Engineering, K. S. Rangasamy Institute of Technology, Tiruchengode, TN, India
[5]Department of Electrical & Electronics Engineering, Nandha College of Technology, Perundurai, TN, India
[6]Department of Mechanical Engineering, Nandha College of Technology, Perundurai, TN, India
Received: 12.06.2026 Accepted: 14.07.2026 Published: 30.09.2026
*vpsuresh4@gmail.com

ABSTRACT

This study presents a detailed investigation of the physicochemical characteristics and photocatalytic performance of copper oxide and titanium dioxide nanoparticles prepared through conventional sol–gel and phytochemical-assisted routes. The chemically synthesized samples are denoted as (CuO)c and (TiO_2)c, while the biomediated products obtained using pomegranate peel extract are represented as (CuO)gs and (TiO_2)gs. X-ray diffraction analysis confirms the successful formation of monoclinic and tetragonal crystalline structures for the copper-based and titanium-based oxide nanomaterials, respectively. Incorporating plant-derived reducing and stabilizing agents does not significantly alter the lattice parameters. Fourier-transform infrared spectroscopy confirms the formation of metal–oxygen bonding networks and also indicates surface hydroxyl functionalities, which contribute to enhanced photocatalytic activity. Optical investigations reveal an increase in the band-gap energy of copper-based oxide from 1.89 eV to 2.58 eV after green synthesis, whereas a reduction in the band-gap energy from 3.02 eV to 2.82 eV is observed for titanium-based oxide. Photoluminescence measurements show predominantly blue emission for both copper- and titanium-based nanostructures, indicating radiative recombination involving band-edge and defect-related electronic states. The photocatalytic behavior of (CuO)c and (CuO)gs toward indigo carmine degradation under ultraviolet illumination was evaluated, yielding degradation efficiencies of 55% and 69%, respectively, after 180 min. Similarly, under identical irradiation conditions, removal of Congo red dye reached 93% for (TiO_2)c and 82% for (TiO_2)gs after 180 min. Scavenger-assisted experiments identified the active species involved in the degradation pathways of indigo carmine and Congo red. Furthermore, recyclability assessments over five consecutive cycles demonstrated the stability and reusability of the synthesized photocatalysts. The observed photocatalytic responses were interpreted based on the proposed charge-generation, migration, and reactive-radical formation mechanisms.

Keywords: Photocatalytic performance; Congo red; Photoluminescence; Band-gap energy; UV illumination.

1. INTRODUCTION

Discharging untreated textile effluents containing toxic pollutants and synthetic dyes poses a serious threat to human health and aquatic ecosystems. Consequently, green-synthesized metal oxide photocatalysts have attracted considerable attention for sustainable wastewater treatment owing to their excellent stability, strong oxidation capability, and efficient pollutant degradation performance (Arulnangai *et al.* 2025). Bio-derived adsorbent materials have demonstrated considerable potential for the removal of dye pollutants from aqueous environments through efficient surface interactions and environmentally sustainable treatment approaches, highlighting the importance of low-cost materials for wastewater remediation (Rajesh *et al.* 2024; Gaddala *et al.* 2025). Sustainable carbon-based materials derived from agricultural biomass have attracted significant attention for environmental remediation owing to their high surface area, adsorption capability, and eco-friendly nature, making them promising candidates for water purification applications (Kumar *et al.* 2026). Green-synthesized metal oxide nanoparticles have emerged as promising photocatalysts for the sustainable degradation of dye pollutants in wastewater (Nagajyothi *et al.* 2020). Nanomaterials such as TiO_2, ZnO, Fe_3O_4, and CuO have demonstrated remarkable potential for wastewater treatment through adsorption, photocatalysis, membrane filtration, and antimicrobial mechanisms, offering sustainable solutions for environmental remediation (Al-Maliki *et al.* 2026). TiO_2, ZnO, and CuO nanoparticles

exhibited excellent photocatalytic performance, achieving up to 100% dye degradation under visible-light irradiation, with ZnO and CuO systems showing degradation efficiencies of approximately 99% and 95%, respectively (Gupta *et al.* 2023).

Gd^{3+}-substituted bismuth ferrite ($BiFeO_3$) nanoparticles exhibited enhanced visible-light photocatalytic performance, increasing indigo carmine degradation from 34% to 69% and Congo red degradation from 37% to 73%, owing to improved porosity and a redshift in the band gap (Basavarajappa *et al.* 2018). Helium ion-modified tungsten trioxide (WO_3) microparticles exhibited significantly improved photocatalytic performance, achieving complete Indigo Carmine degradation and enhanced Congo red removal compared to untreated WO_3 (Kozlovskiy and Zdorovets, 2020).

Heterojunction engineering and green synthesis strategies have been widely employed to enhance charge separation, visible-light absorption, and photocatalytic performance of metal oxide semiconductors for water purification applications (Leishangthem *et al.* 2025). CeO_2–CuO–TiO_2 ternary nanostructures exhibited enhanced visible-light photocatalytic activity due to synergistic interactions among the constituent oxides, achieving 62.9% degradation of organic contaminants within 90 min, which outperformed commercial TiO_2 photocatalysts (Deganello *et al.* 2025). The CuO@TiO_2 nanocomposite showed enhanced visible photocatalytic activity due to improved charge separation and a reduced band gap energy. The photocatalyst achieved complete degradation of Acid Yellow 36 under simulated sunlight irradiation. The photocatalyst also effectively treated actual textile wastewater (Wang *et al.* 2023). Incorporating CuO reduced the band gap of TiO_2 nanofibers from 3.04 to 2.66 eV, while decreased photoluminescence intensity confirmed improved charge-carrier separation and transfer (Wen *et al.* 2022). The CuO–TiO_2–HNT photocatalyst achieved 82% degradation of Congo red dye within 2.5 h under visible-light irradiation. Degradation followed a pseudo-first-order kinetic model with a constant rate of 0.01866 min^{-1}. The enhanced activity was attributed to efficient charge separation through the Z-scheme heterojunction (Pouthika and Madhumitha, 2025).

Pomegranate peel extract has also been utilized in the preparation and surface modification of iron-oxide-based nanocomposites for azo dye degradation, demonstrating its potential for environmentally sustainable wastewater-treatment applications (Iranfar *et al.* 2021). Plant-mediated metal oxide nanoparticles, including TiO_2, ZnO, and CuO, have demonstrated significant potential for sustainable photocatalytic degradation of dye pollutants through eco-friendly synthesis approaches (Mallah *et al.* 2025). CuO–TiO_2 nanocomposites were green-synthesized using *Hibiscus sabdariffa* flower extract by combining CuO and TiO_2 nanoparticles through a plant-mediated co-precipitation approach, where phytochemicals acted as reducing and stabilizing agents (Meli *et al.* 2025). The reduced band gap energy observed for the synthesized photocatalyst indicates enhanced light absorption and photocatalytic activity. A similar enhancement in optical properties was reported for pomegranate peel extract-mediated SnO_2/Fe_3O_4 nanocomposites, where band gap reduction improved photocatalytic degradation efficiency under irradiation (Azizi *et al.* 2025). Pomegranate peel extract-mediated ZnO nanoparticles demonstrated efficient photocatalytic degradation of MB dye. The photocatalyst achieved a degradation rate constant of 0.065 min^{-1}, indicating rapid kinetic reaction. This enhanced performance was attributed to improved charge transport and light-absorption characteristics (Djafarou *et al.* 2026). Pomegranate peel-derived reduced graphene oxide (rGO)/Co nanohybrids exhibited excellent photocatalytic activity toward methylene blue degradation, highlighting the potential of green-synthesized nanomaterials for environmental remediation (Ben *et al.* 2024). FESEM analysis revealed the successful formation of pomegranate peel extract-mediated Ag nanoparticles with particle sizes ranging from 57.7 to 142.4 nm, indicating effective stabilization and dispersion by the phytoconstituents of the extract (Joshi *et al.* 2018). The CuO@A-TiO_2/Ro-TiO_2 achieved complete degradation of Reactive Orange 16 dye within 100 min under sunlight irradiation. This improved photocatalytic activity was attributed to synergistic interactions between CuO and TiO_2. The nanocomposite also demonstrated excellent performance in treating real textile wastewater (Nassar *et al.* 2024). Green-synthesized CuO/TiO_2 nanocomposites exhibited a reduced band gap and achieved excellent photocatalytic degradation efficiencies toward methylene blue and Congo red dyes, demonstrating their potential for visible-light-driven wastewater treatment (Pamitha *et al.* 2026).

The study focuses on synthesizing copper-based and titanium-based oxide nanoparticles (NPs) through a phytochemical-assisted sol–gel route, using pomegranate peel-derived bioactive compounds as reducing and stabilizing agents. For comparative evaluation, identical nanomaterials were also produced using a conventional chemical sol–gel approach. The resulting nanostructures were systematically characterized for crystallinity, lattice characteristics, vibrational behavior, surface functional groups, optical response, charge-carrier recombination, and morphological features. In addition, their photocatalytic efficiencies toward the degradation of Congo red dyes and indigo carmine under ultraviolet irradiation were assessed. Furthermore, radical-trapping investigations were performed to identify the dominant reactive species involved in the degradation pathway and elucidate the underlying photocatalytic mechanism.

2. EXPERIMENTAL METHODOLOGY

2.1 Synthesis of Plant Extract

The plant-derived precursor was first subjected to a purification process to eliminate surface contaminants and unwanted residues. Fresh pomegranate peels were cut into small fragments and thoroughly rinsed using a deionized water–ethanol mixture (1:2), followed by ultrasonication for 30 min. The cleaned material was subsequently filtered and oven-dried for 1 day. Approximately 5 g of the dried peel was finely ground and dispersed in 100 mL of deionized water. The suspension was heated at 70 °C for 120 min and cooled naturally to ambient temperature, then filtered to obtain the bioactive extract for further synthesis.

2.2 Chemical Preparation of (CuO)c and (TiO_2)c NPs

Copper- and titanium-based oxide NPs were synthesized through a conventional sol–gel route using copper nitrate trihydrate [$Cu(NO_3)_2 \cdot 3H_2O$, ACS reagent, ≥98%] and titanium(IV) isopropoxide [$Ti(OCH(CH_3)_2)_4$, ≥97%] as precursor materials. A 0.5 M precursor solution was prepared under continuous magnetic stirring for 1 h to ensure complete homogenization. Subsequently, 0.9 M NaOH solution was added dropwise with vigorous stirring until the pH reached 11. The reaction mixture was stirred for 2 h after alkali addition, then left undisturbed overnight for aging. The clear supernatant was carefully decanted, while the remaining suspension was centrifuged for 10 min. The obtained precipitates were washed three times with deionized water and ethanol to eliminate residual impurities, dried at 110 °C in air, and finally calcined at 500 °C to obtain chemically synthesized NPs, denoted as (CuO)c and (TiO_2)c.

2.3 Green Synthesis of (CuO)gs and (TiO_2)gs NPs

For bio-assisted synthesis, 0.5 M precursor solutions of copper nitrate or titanium precursor were mixed with 1 mL of pomegranate peel extract and 7 mL of distilled water. The resulting mixture was vigorously stirred while 1 M NaOH solution was added dropwise. A gradual color change was observed after 1 h, indicating the initiation of nanoparticle formation. Stirring was continued for an additional 3 h to facilitate complete growth of the nanostructures. The appearance of dark brown and pale white precipitates confirmed the formation of copper-based and titanium-based oxide NPs, respectively. Previous studies have demonstrated the green synthesis of CuO and TiO_2 NPs using plant extracts as reducing and stabilizing agents, followed by calcination (Bopape *et al.* 2023). The products were collected by centrifugation, dried at 110 °C, and subsequently calcined at 500 °C to obtain the green-synthesized nanoparticles, designated as (CuO)gs and (TiO_2)gs.

Fig. 1: Bio-assisted synthesis of CuO and TiO_2 NPs

2.4 Characterization of Photocatalysts

XRD was carried out at ambient temperature using a Bruker D8 Advance. FT-IR spectroscopy was performed using an infrared spectrophotometer (Shimadzu IRTracer-100 spectrometer). UV reflectance was obtained using a UV spectrophotometer (Shimadzu UV-2600 UV–Vis spectrophotometer). SEM images were acquired using a ZEISS GEMINI Scanning Electron Microscope. Zeta potential was measured by a dynamic light scattering instrument (Anton Paar). PL spectra were acquired using a PerkinElmer LS 55 luminescence spectrometer.

2.5 Photocatalytic Activity

Photocatalytic efficiency of synthesized nanomaterials was evaluated using indigo carmine dye as the target pollutant. The physicochemical properties of selected dyes were summarized in Table 1. Photocatalytic experiments were conducted in a cylindrical quartz batch reactor under ambient conditions, with continuous magnetic stirring and aeration supplied through an air-diffusion system to ensure uniform suspension of catalyst particles throughout the reaction period.

Table 1. Physicochemical properties of the dye pollutants employed in the photocatalytic degradation experiments

Dye	Color	CAS ID	MW (g/mol)	λ_{max} (nm)
Congo red	Red	573-58-0	696.66	498
Indigo carmine	Blue	860-22-0	466.35	610

Approximately 100 mL of 25 mg/L dye solution with 0.1 g of photocatalyst was kept in the dark for 25

min to allow adsorption–desorption between the catalyst surface and dye molecules. Subsequently, the suspension was exposed to ultraviolet irradiation (8 W, λ_{max} = 254 nm). The 5 mL aliquots were filtered and withdrawn to eliminate suspended particles. The variation in dye concentration was determined from absorbance measured at the characteristic wavelength (λ_{max}) using a UV–Vis spectrophotometer. The percentage degradation efficiency (D) was calculated using Eq. (1):

$$D\ (\%) = \frac{C_o - C_t}{C_o} \times 100 \qquad \ldots (1)$$

where C_o represents the initial concentration of the dye solution, while C_t corresponds to the residual dye concentration measured at an irradiation period of t min.

2.6 Radical Scavenger Experiment

To identify the dominant reactive species in the photocatalytic process, radical-trapping experiments were performed during dye degradation. In these tests, ammonium oxalate (AO), tert-butanol (t-BuOH), and 1,4-benzoquinone (BQ) were introduced individually as selective scavengers for hydroxyl radicals, photogenerated holes, and superoxide radicals. For each experiment, 100 mL of 25 ppm dye solution was combined with 0.1 g of photocatalyst and 10 mM of the desired scavenging agent. Following the establishment of adsorption–desorption equilibrium, suspensions were irradiated with ultraviolet light. Degradation efficiencies obtained in the presence of all scavengers were subsequently analyzed to evaluate the contributions of corresponding species to the photocatalytic mechanism.

3. RESULTS AND DISCUSSION

3.1 Physical Characterization

3.1.1 Crystal Structure Study

To examine the crystalline characteristics of the synthesized samples, X-ray diffraction patterns of (CuO)c and (CuO)gs are presented in Fig. 2. Both specimens exhibit well-defined diffraction peaks at approximately 32.5°, 35.5°, 38.7°, 48.8°, 53.5°, 58.3°, 61.5°, 66.2°, 68.1°, 72.4°, and 75.1°. These reflections correspond to (110), (−111), (111), (−202), (020), (202), (−113), (−311), (220), (311), and (004) crystallographic planes. Phase identification using the Search-Match software confirms that the observed diffraction peaks were consistent with the monoclinic structure of copper oxide. The absence of secondary phases indicates successful formation of highly crystalline NPs. Furthermore, diffraction data show good agreement with previously reported studies.

As shown by the diffraction profiles, both synthesized samples exhibit well-defined crystallinity. Moreover, no impurity peaks or secondary crystalline phases were detected following the bio-assisted synthesis route, confirming the phase purity of the obtained nanostructures. Detailed structural refinement reveals only minor variations in the lattice parameters between the chemically prepared and green-synthesized specimens.

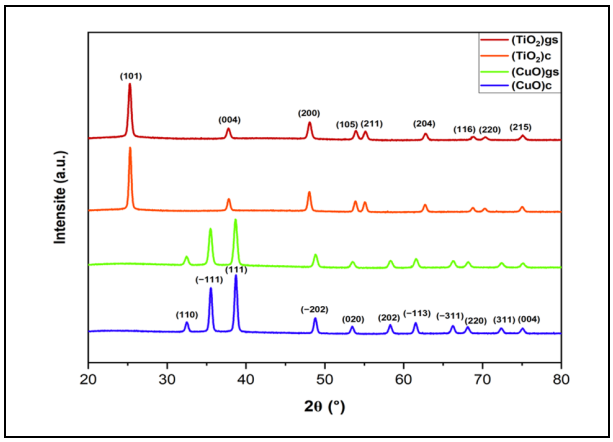

Fig. 2: XRD patterns of (CuO)c, (CuO)gs, (TiO_2)c, and (TiO_2)gs nanomaterials

Average crystallite size (D) was calculated using the Scherrer equation (Eq. 2).

$$D = \frac{K\lambda}{\beta \cos\theta} \qquad \ldots (2)$$

where K is the shape factor (0.89), β is the full width at half maximum of the selected diffraction peak, λ is the X-ray wavelength (0.15418 nm), and θ is the Bragg diffraction angle. Average crystallite sizes calculated using the Scherrer equation were 23.59 nm and 23.01 nm for (CuO)c and (CuO)gs, respectively. The negligible difference in crystallite size indicates that the green synthesis approach did not significantly influence crystal growth and preserved the crystalline characteristics of CuO NPs. Table 2 summarizes the calculated crystallite sizes.

The diffraction patterns of (TiO_2)c and (TiO_2)gs are also presented in Fig. 2. Phase analysis using Search-Match software confirms that the diffraction peaks correspond to the tetragonal anatase structure (JCPDS card No. 21-1272, space group $I4_1/amd$). For (TiO_2)c, prominent reflections were observed at approximately 25.3°, 37.8°, 48.0°, 53.9°, 55.1°, 62.7°, 68.8°, 70.3°, and 75.0°, corresponding to (101), (004), (200), (105), (211), (204), (116), (220), and (215) crystallographic planes. The bio-assisted synthesis route does not alter the crystal structure or significantly affect lattice parameters, as listed in Table 2. Furthermore, no impurity-related reflections were detected, indicating the formation of phase-pure nanoparticles. The sharp, intense diffraction peaks confirm high crystallinity in both samples. The average crystallite sizes are 21.5 and 18.8 nm for (TiO_2)c and (TiO_2)gs, respectively, indicating an approximately

12.6% reduction after green synthesis. These structural characteristics are consistent with previously reported findings for titanium-based oxide NPs. The diffraction peaks of (TiO_2)c and (TiO_2)gs were indexed to the tetragonal anatase phase (JCPDS No. 21-1272), consistent with high-crystallinity, phase-pure TiO_2 formation. In comparison, TiO_2 in CuO–TiO_2 composite systems has been reported to crystallize as rutile, with TiO_2 NPs homogeneously distributed over CuO surfaces, indicating effective composite formation and strong interfacial interaction between the two metal oxides (Baran *et al.* 2022).

Table 2. Structural refinement results including interaxial angles (α, β, γ), lattice constants (a, b, c), average crystallite size (D), and unit-cell volume (V) of synthesized nanoparticles

Sample	Average Crystallite Size, D (nm), XRD	a (A°)	b (A°)	c (A°)	α (°)	β (°)	γ (°)	Unit-cell Volume, V $(A°)^3$	Crystal Structure
(CuO)c	23.59	4.684	3.425	5.129	90	99.54	90	81.1	Monoclinic
(CuO)gs	23.01	4.684	3.425	5.129	90	99.54	90	81.1	Monoclinic
(TiO_2)c	21.50	3.784	3.784	9.514	90	90	90	136.2	Tetragonal Anatase
(TiO_2)gs	18.80	3.784	3.784	9.514	90	90	90	136.2	Tetragonal Anatase

3.1.2 Lattice Vibration Study

To identify surface chemical functionalities and bonding characteristics of synthesized copper-based and titanium-based oxide nanomaterials, FT-IR spectroscopy was performed over the spectral range of 4000–400 cm^{-1}. Fig. 3 shows the corresponding FT-IR spectra of the prepared samples.

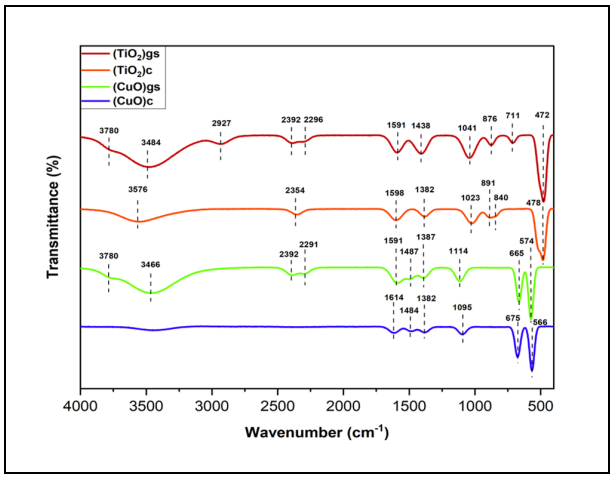

Fig. 3: FT-IR spectra of (CuO)c, (CuO)gs, (TiO_2)c, and (TiO_2)gs NPs

The FT-IR spectra of the copper oxide NPs reveal several characteristic absorption bands, with the green-synthesized sample showing more detectable surface functionalities (Table 3). Strong absorption bands observed at approximately 566–675 cm^{-1} for (CuO)c and 574–665 cm^{-1} for (CuO)gs were attributed to the Cu–O lattice, confirming successful formation of CuO NPs. The green-synthesized sample also shows broad absorptions centered at 3780 cm^{-1} and 3466 cm^{-1}, corresponding to O–H groups of adsorbed surface hydroxyls and water molecules. Bands observed at 1591, 1487, 1387, and 1114 cm^{-1} are associated with residual phytochemical species adsorbed on the nanoparticle surface. In comparison, the chemically synthesized sample displays weaker absorption bands at 1614, 1484, 1382, and 1095 cm^{-1}. The appearance of additional absorption at 2391 and 2291 cm^{-1} in the green-synthesized sample further suggests interactions between bioactive compounds and the nanoparticle surface (Fig. 3). Overall, the broader absorption bands and increased number of vibrational features observed for (CuO)gs indicate surface modification by phytochemical constituents present during the green synthesis process.

For the titanium-based oxide NPs, the FT-IR spectra in Fig. 3 show characteristic absorption bands in the 400–800 cm^{-1} region, confirming the formation of Ti–O and Ti–O–Ti bonding networks. A prominent absorption band at approximately 1041 cm^{-1} is observed for (TiO_2)gs, which may be C–N and C–O stretching associated with residual phytochemical species (Table 3). The corresponding band in (TiO_2)c appears at approximately 1023 cm^{-1} with lower intensity. Both samples show absorption bands around 1591–1598 cm^{-1}, assigned to H–O–H vibrations of adsorbed water molecules. The green-synthesized sample additionally displays bands at 1438, 876, and 711 cm^{-1}, whereas the chemically synthesized sample shows bands at 1382, 891, and 840 cm^{-1}. A weak absorption band at 2927 cm^{-1} was observed only for (TiO_2)gs, indicating the presence of trace aliphatic organic groups originating from the plant extract. Broad absorption bands centered at approximately 3484 cm^{-1} for (TiO_2)gs and 3576 cm^{-1} for (TiO_2)c correspond to O–H stretching of adsorbed

moisture and surface hydroxyl groups. These hydroxyl groups enhance photocatalytic activity by facilitating the formation of reactive hydroxyl radicals. The broader and more intense O–H absorption band observed for (TiO_2)gs suggests enhanced surface hydroxylation resulting from the phytochemical-mediated synthesis process. These FTIR assignments are consistent with previous reports on green-synthesized Cu-doped TiO_2 nanostructures. Comparable metal–oxygen bonds (Cu–O, Cu–O–Ti–O) were reported at 833 and 672 cm^{-1} in copper-doped TiO_2 NPs synthesized using *Beta vulgaris* leaf extract, confirming successful metal–oxide bond formation through phytochemical-mediated synthesis (Surendra *et al.* 2025).

Table 3. FT-IR band assignments and corresponding functional groups identified in the synthesized nanoparticles

No.	(CuO)c	(CuO)gs	Assignment	(TiO_2)c	(TiO_2)gs	Assignment
1	566	574	Cu–O lattice stretching vibration	478	472	Ti–O–Ti lattice vibration
2	675	665	Cu–O lattice stretching vibration	_	711	Ti–O–Ti / Ti–O vibration
3	1095	1114	C–N/C–O stretching vibration	1023	1041	C–O/C–N stretching vibration
4	1382	1387	C–O stretching vibration	1382	1438	C–N stretching / aromatic ring vibration
5	1484	1487	Aromatic skeletal vibration / C–O stretching	1598	1591	H–O–H bending vibration
6	1614	1591	H–O–H bending vibration of adsorbed water	–	–	–
7	–	2291	Adsorbed atmospheric CO_2 vibration	2354	2296	Adsorbed atmospheric CO_2 vibration
8	–	2391	Adsorbed atmospheric CO_2 vibration	–	2392	Adsorbed atmospheric CO_2 vibration
9	–	3466	O–H stretching vibration	3576	3484	O–H stretching vibration
10	–	3780	Surface hydroxyl (–OH) stretching	–	3780	Surface hydroxyl (–OH) stretching
11	–	–	–	–	2927	Aliphatic C–H stretching from phytochemical residues

3.1.3 Optical Study

The UV–Vis reflectance spectra of chemically synthesized and green-synthesized copper- and titanium-based oxide NPs, over the wavelength range of 200–800 nm, are presented in Fig. 4.

For the copper-based oxide NPs, a single dominant reflectance maximum is observed, with λ_{max} values located at 254 and 250 nm for the chemically synthesized and green-synthesized samples. In contrast, the titanium-based oxide NPs exhibit two characteristic absorption features, appearing at approximately 225 and 482 nm for the chemically prepared sample and 245 and 455 nm for the bio-assisted sample. To evaluate the optical absorption behavior, the reflectance data were converted into a quantity proportional to the absorption coefficient by the Kubelka–Munk function, $F(R\infty)$ (Eq. 3). For comparison, green-synthesized AgNPs have been reported to exhibit a distinct surface plasmon resonance peak at approximately 407 nm, demonstrating the characteristic optical response of plant-mediated metallic nanoparticles (Mehata, 2021).

$$F(R\infty) = (1 - R\infty)^2/(2R\infty) = k/s \quad \ldots (3)$$

where k represents the absorption coefficient, s corresponds to the scattering coefficient, and R denotes measured diffuse reflectance, which is generally considered to be nearly wavelength-independent.

According to the Tauc method:

$$\alpha h\nu = A(h\nu - E_g)^n \quad \ldots (4)$$

where h denotes Planck's constant, ν is the frequency of the incident photon, A is the material-dependent proportionality constant, n denotes the exponent associated with the nature of the electronic transition, and α corresponds to the optical absorption coefficient.

So, the Tauc relation can be written as:

$$F(R\infty)h\nu = A(h\nu - E_g)^n \quad \ldots (5)$$

Optical band-gap energies (E_g) of chemically synthesized and green-synthesized copper- and titanium-based oxide nanoparticles were determined from Tauc plots of $[F(R\infty)h\nu]^2$ vs. photon energy ($h\nu$), presented in

Fig. 5. For copper-based oxide samples, the estimated band-gap energy increases from 1.89 eV for (CuO)c to 2.58 eV for (CuO)gs. This range is consistent with reports for similar copper oxide nanostructures. In contrast, the titanium-based oxide nanoparticles exhibit a reduction in band gap from 3.02 eV for (TiO_2)c to 2.82 eV for (TiO_2)gs following bio-assisted synthesis. This decrease is associated with the generation of defect-related localized energy levels and surface states, which enhance visible-light absorption and facilitate band-gap narrowing characteristics. In previous studies, the band gap of the synthesized photocatalyst may enhance visible-light absorption and photocatalytic efficiency, consistent with the findings reported for green-synthesized CuO NPs exhibiting a band gap of 1.35 eV (Pamitha *et al.* 2025).

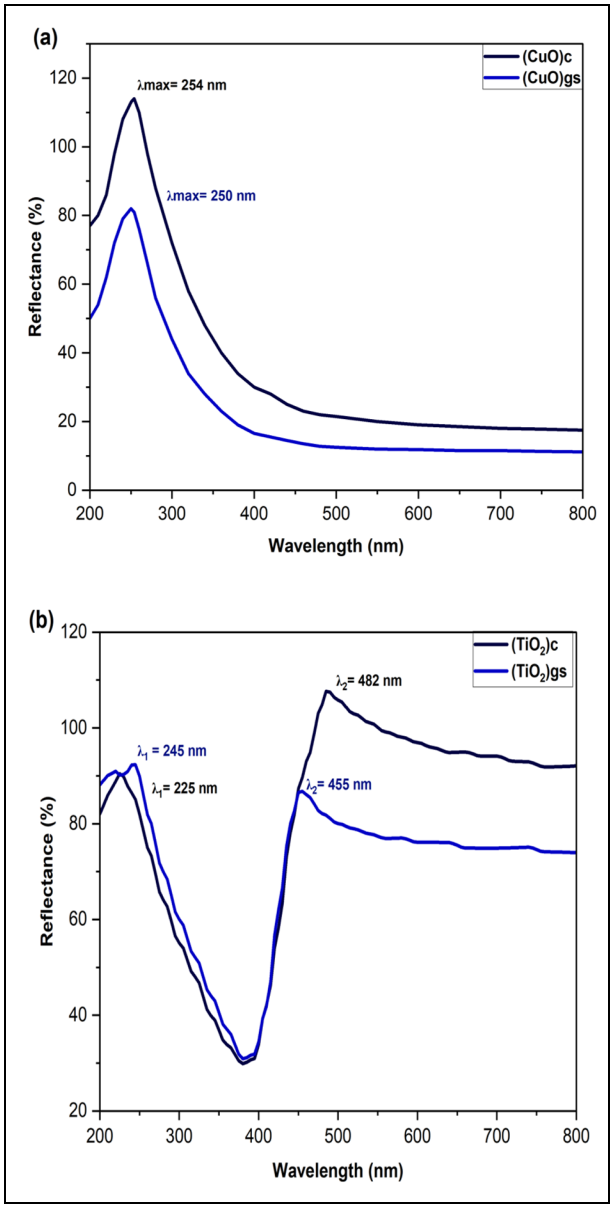

Fig. 4: UV–Vis diffuse reflectance spectra of (a) (CuO)c and (CuO)gs NPs and (b) (TiO_2)c and (TiO_2)gs NPs

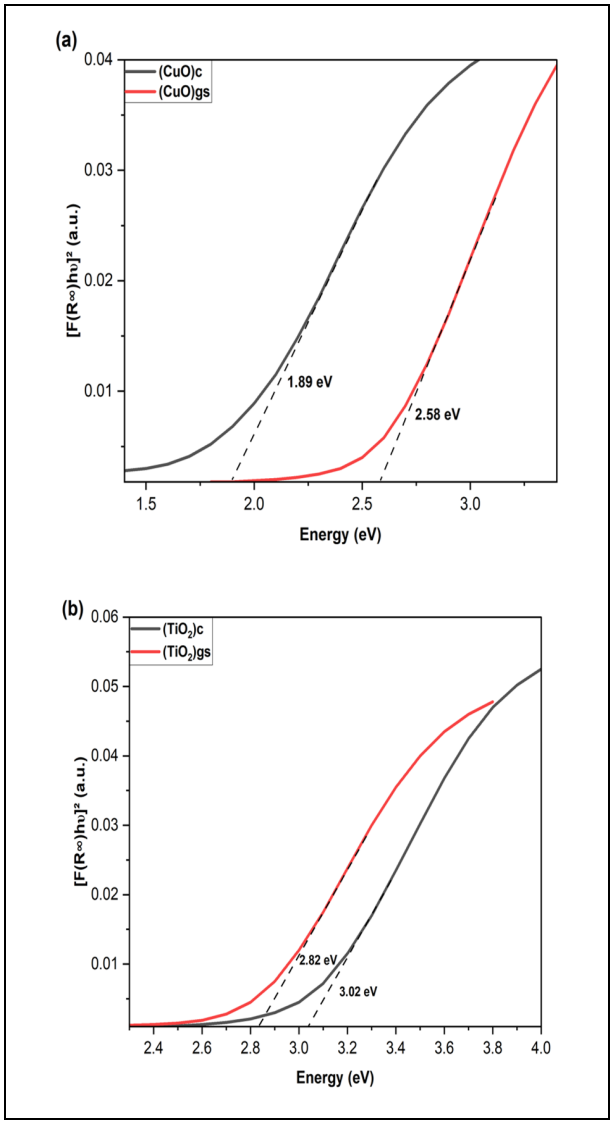

Fig. 5: Tauc plots for optical band-gap determination of (a) (CuO)c and (CuO)gs NPs and (b) (TiO_2)c and (TiO_2)gs NPs

3.1.4 Photoluminescence Study

Photoluminescence (PL) spectroscopy is a valuable technique for examining the electronic and optical behavior of semiconductor nanomaterials. When the material is irradiated with photons possessing energy greater than the band–gap energy, electron–hole pairs are generated. These charge carriers subsequently recombine through different pathways, including band-to-band transitions, free-exciton recombination, and defect- or impurity-related states, resulting in photon emission. PL analysis is widely employed to evaluate migration, charge-carrier trapping, transfer, and recombination characteristics. Since the separation efficiency of photogenerated holes and electrons strongly influences photocatalytic performance, PL measurements provide important information regarding photocatalyst activity. Fig. 6 shows the PL spectra of copper oxide and titanium dioxide NPs. Both materials exhibit distinct, well-

defined emission bands. The maximum emission wavelengths are centered at approximately 448 nm and 440 nm for (CuO)c and (CuO)gs, respectively, while (TiO_2)c and (TiO_2)gs exhibit emission maxima at 428 nm and 420 nm, respectively. The emitted radiation originates from the recombination of trapped charge carriers, where the photon energy corresponds to the energy difference between the initial and final electronic states involved in the transition near the valence-band region. A previous study reported that PL analysis revealed enhanced visible-light absorption and effective charge separation in Cu/N-TiO_2 due to strong electronic interactions between CuO and N-TiO_2, contributing to superior photocatalytic performance and stability (Mancuso *et al.* 2023).

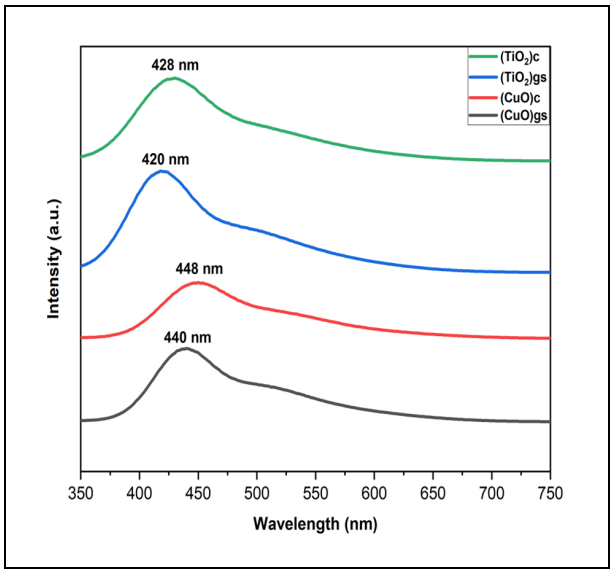

Fig. 6: Photoluminescence spectra of (CuO)c, (CuO)gs, (TiO_2)c, and (TiO_2)gs NPs

Table 4 summarizes the emission peak positions of the synthesized nanoparticles along with their corresponding optical band-gap energies. The emission bands observed for the chemically synthesized and green-synthesized copper-based oxide samples correspond to blue and blue luminescence, respectively. In contrast, both the chemically prepared and bio-assisted titanium-based oxide NPs predominantly exhibit blue emission, indicating defect-related radiative recombination centers within the nanostructures.

Each emission wavelength corresponds to a particular radiative recombination pathway associated with specific defect states distributed within the forbidden energy region. Based on the estimated band-gap energies, the chemically synthesized and green-synthesized copper-based oxide NPs predominantly exhibit band-to-band recombination behavior. In contrast, the titanium-based oxide samples display recombination involving localized defect states. This behavior may arise from trapping centers generated by lattice imperfections and structural defects located between the Fermi level and the conduction band. Previous studies have reported that visible-light emission in titanium-based oxide nanostructures within the 420–428 nm range is commonly associated with oxygen vacancies and interstitial defect sites. The intensity and shape of the PL spectrum are strongly influenced by the microstructural characteristics of the material, particularly particle size. Generally, reducing particle size widens the band gap because of quantum confinement effects. In previous studies, the TiO_2–0.1La_2O_3–0.2CuO nanocomposite showed enhanced photocatalytic activity, reducing the band gap from 3.23 to 2.27 eV and attaining more than 95% brilliant green dye degradation within 204 min under visible light (Boudraa *et al.* 2024).

The conductivity and zeta potential values of nanoparticles are summarized in Table 4. Zeta potential is an important parameter for colloidal stability, as values exceeding approximately ±25 mV promote electrostatic repulsion and reduce particle aggregation. Likewise, conductivity influences particle dispersion behavior in suspension. Higher conductivity can improve the uniform distribution of nanoparticles and minimize agglomeration, thereby enhancing the stability and reproducibility of the colloidal system.

Table 4. Photoluminescence emission characteristics, optical band-gap energies, zeta potential, conductivity, and particle size of synthesized nanoparticles

Sample	Peak Position (eV)	Emission Color	E_g (eV)	Zeta Potential (mV)	Conductivity (mS/cm)	Dynamic Light Scattering (DLS) Diameter (nm)
(CuO)c	2.77 (448 nm)	Blue	1.89	-9.86	0.084	95.4
(CuO)gs	2.82 (440 nm)	Blue	2.58	-20.6	0.063	71.3
(TiO_2)c	2.90 (428 nm)	Blue	3.02	-48.8	0.077	65.5
(TiO_2)gs	2.95 (420 nm)	Blue	2.82	-42.7	0.385	58.6

3.2 Photocatalytic Analysis

3.2.1 Photocatalytic Analysis of CuO NPs

The photocatalytic performance of (CuO)c and (CuO)gs was evaluated through the degradation of indigo carmine (IC) dye (25 ppm) using 1 g/L of photocatalyst under UV irradiation for 180 min. As illustrated in Fig. 7, an adsorption–desorption equilibrium period of 40 min was established before illumination. The adsorption efficiencies were approximately 40% and 38% for (CuO)c and (CuO)gs, respectively. High adsorption capacity facilitates close contact between the catalyst surface and dye molecules, thereby enhancing photocatalytic oxidation under light exposure. During the initial 60 min of irradiation, photocatalytic activity dominated degradation. Subsequently, the degradation rate of (CuO)c gradually declined after nearly 80 min of exposure. This behavior was due to the accumulation of dye molecules on the catalyst surface, which limits light penetration and reduces the efficiency of photogenerated charge carriers.

After 180 min of UV irradiation, degradation efficiency reached 69% for (CuO)gs and 55% for (CuO)c. The superior efficiency of the green-synthesized sample was associated with its larger lattice parameter, higher band-gap energy, and increased zeta potential value compared with the chemically synthesized counterpart (Table 4). Elevated zeta potential improves particle stability, dispersion, and interfacial charge-transfer processes in aqueous media, thereby promoting photocatalytic activity.

These characteristics favor electron–hole pair generation during irradiation. In addition, the green-synthesized sample exhibits a higher concentration of surface hydroxyl groups, which readily react with photogenerated holes to form highly oxidative hydroxyl radicals, thereby accelerating the degradation of dye molecules. Previous studies reported that the CuO–Cu_2O–ZnO photocatalyst achieved nearly complete MB degradation under visible-light irradiation. Reduced photoluminescence intensity indicated charge separation, while ZnO incorporation lowered the activation energy from 17.7 to 8.8 kJ mol^{-1}. Enhanced photocatalytic performance was primarily driven by hydroxyl radical formation (Sabzehei *et al.* 2020).

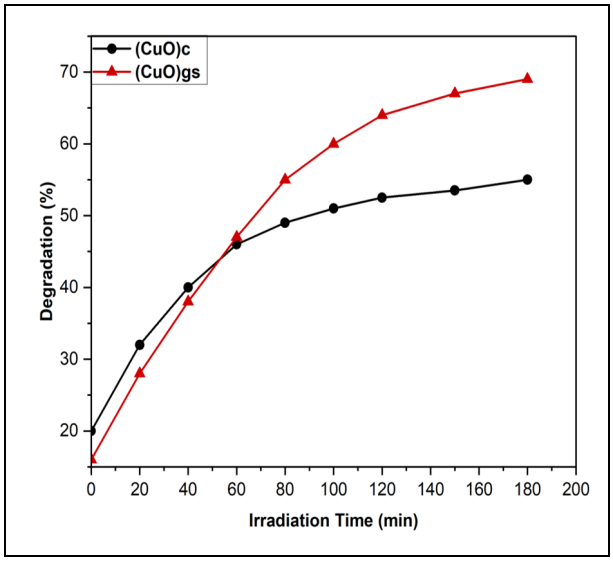

Fig. 7: Photodegradation of indigo carmine dye using 1 g/L of (CuO)c and (CuO)gs photocatalysts under UV irradiation

Fig. 8 presents the photocatalytic degradation behavior of indigo carmine by green-synthesized CuO NPs in the absence and presence of different scavenging agents. After 180 min of irradiation, degradation efficiency reached 71% in the control experiment, while it decreased to 67%, 65%, and 50% with AO, t-BuOH, and BQ. The introduction of 1,4-benzoquinone (BQ) resulted in the most pronounced decrease in degradation efficiency, whereas tert-butanol (t-BuOH) and ammonium oxalate (AO) produced only moderate changes in photocatalytic performance.

These observations indicate that superoxide radicals play a dominant role in the degradation pathway of indigo carmine dye, while hydroxyl radicals (OH) and photogenerated holes (h^+) play a lesser role. The results therefore suggest the photocatalytic process was primarily governed by the generation and participation of superoxide radical species on the catalyst surface. In previous studies, CuO-based heterojunction photocatalysts have demonstrated remarkable dye removal capability, with CuO–Fe_2O_3@Chitin nanocomposites achieving 96.4% indigo carmine degradation under optimized conditions, highlighting the beneficial role of CuO in promoting photocatalytic activity (Alanazi *et al.* 2026).

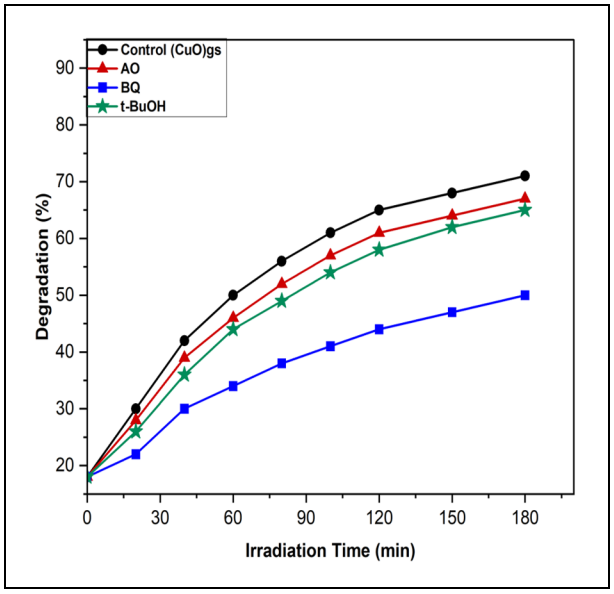

Fig. 8: Photodegradation of indigo carmine dye under UV irradiation using (CuO)gs photocatalyst in the absence and presence of radical scavengers (AO, BQ, and t-BuOH)

3.2.2 Photocatalytic Efficiency of TiO_2 NPs

Photocatalytic activity of chemically synthesized and green-synthesized titanium-based oxide NPs was evaluated towards the degradation of Congo red dye at an initial concentration of 25 ppm. The experiments used a catalyst dosage of 1 g/L under UV irradiation for 180 min, and Fig. 9 shows the corresponding degradation profiles.

To assess the influence of dye adsorption on photocatalytic performance, the reaction mixture was initially kept in the dark for 25 min to reach adsorption–desorption equilibrium. Upon UV irradiation, the catalyst with superior adsorption behavior also showed improved photocatalytic activity, facilitating the conversion of dye molecules into less harmful products. After 180 min of UV irradiation, degradation efficiencies reached approximately 93% and 80% for (TiO_2)c and (TiO_2)gs, respectively. This behavior is consistent with the physicochemical characteristics summarized in Table 4, where the chemically synthesized sample possesses a slightly wider optical band gap of 3.02 eV and a higher absolute zeta-potential value (−48.8 mV), contributing to enhanced colloidal stability and photocatalytic performance.

Zeta potential represents the electrokinetic potential at the interface between the particle surface and the surrounding liquid medium and indicates colloidal stability. Larger absolute zeta-potential values promote stronger electrostatic repulsion among particles, thereby suppressing agglomeration and improving dispersion stability. The higher zeta-potential value of (TiO_2)c enhances nanoparticle dispersion within the dye solution, increasing the number of active sites exposed to incident light and consequently improving photocatalytic efficiency. Furthermore, the relatively lower electrical conductivity of (TiO_2)c compared with (TiO_2)gs may contribute to reduced charge-carrier mobility, thereby suppressing electron–hole recombination and prolonging the lifetime of photogenerated carriers. This effect further supports the superior degradation performance observed for the chemically synthesized sample.

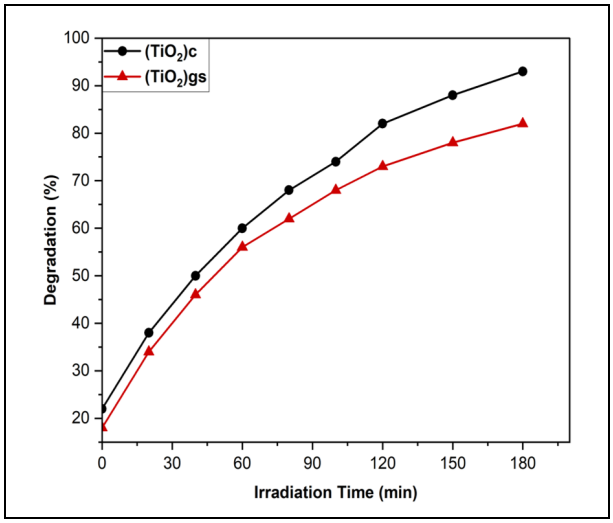

Fig. 9: Photodegradation results of Congo red dye with 1 g/L of (TiO_2)c and (TiO_2)gs photocatalysts under UV irradiation

To identify the active species responsible for Congo red degradation, we performed radical-trapping experiments using chemically synthesized titanium-based oxide NPs. In this study, t-BuOH, BQ, and AO were used as selective scavengers for superoxide radicals, photogenerated holes (h^+), and hydroxyl radicals (•OH). A significant reduction in degradation efficiency in the presence of specific scavengers shows involvement of the corresponding reactive species in the photocatalytic process.

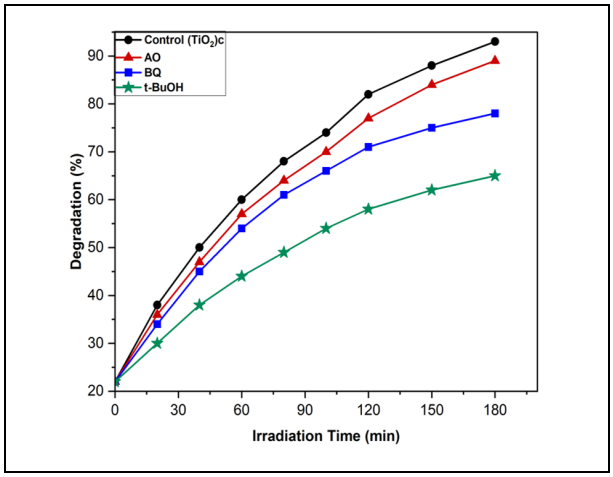

Fig. 10: Photodegradation of indigo carmine dye under UV irradiation with (TiO_2)gs photocatalyst in the absence and presence of radical scavengers

Fig. 10 compares the degradation behavior of Congo red dye in the absence and inclusion of various scavenging agents. After 180 min of irradiation, degradation efficiency reached 93% in the control experiment, whereas it decreased to 89%, 78%, and 65% in the presence of AO, BQ, and t-BuOH. The photocatalytic efficiency decreases markedly when t-BuOH and BQ are introduced into the reaction system, whereas AO exhibits a comparatively smaller influence. These observations suggest that superoxide and hydroxyl radicals are the predominant reactive species governing Congo red degradation, while the contribution of photogenerated holes (h^+) is relatively less significant in the overall photocatalytic mechanism.

3.2.3 Photocatalytic Reaction Mechanisms

Based on the degradation behavior of the investigated dyes, the TiO_2-based oxide NPs exhibited superior activity toward Congo red dye under identical experimental conditions, whereas the copper-based oxide NPs showed better performance for indigo carmine degradation. The difference can be attributed to distinct chemical structures and charge properties of the dye molecules. Congo red is an anionic diazo dye, while indigo carmine exists as an organic sulfonated compound. Interactions between dye molecules and catalyst surfaces play an important role in adsorption efficiency and subsequent photocatalytic efficiency. Previous studies reported that Zn_2Al-LDH selectively adsorbed anionic dyes, achieving a higher uptake capacity for indigo carmine than Congo red through electrostatic interactions with the layered hydroxide surface (Bouteiba *et al.* 2020).

In general, photocatalytic oxidation of organic contaminants proceeds through several sequential steps: (i) absorption of photons by the semiconductor catalyst, (ii) electron–hole pair generation, (iii) charge carriers reacting with adsorbed species, and (iv) participation of reactive species in oxidation–reduction reactions. During these processes, various reactive oxygen species (ROS) are generated and contribute significantly to pollutant degradation, as described in previous studies:

$$M + h\nu \rightarrow e^-_{(CB)} + h^+_{(VB)} \ (M = Cu \text{ or } Ti) \quad \ldots (6)$$

$$h^+_{(VB)} + H_2O \rightarrow H^+ + OH^- \quad \ldots (7)$$

$$h^+_{(VB)} + OH^- \rightarrow \bullet OH \quad \ldots (8)$$

$$e^-_{(CB)} + O_2 \rightarrow O_2\bullet^- \quad \ldots (9)$$

$$O_2\bullet^- + H^+ \rightarrow HO_2\bullet \quad \ldots (10)$$

For Congo red dye, the generated hydroxyl and superoxide radicals actively attack azo (–N=N–) linkages and N, N-dimethyl functional groups, leading to molecular fragmentation and progressive degradation. The oxidation process proceeds rapidly, efficiently disrupting the chromophoric structure responsible for the dye color. Previous investigations of photocatalytic treatment of Congo red using mixed-metal oxide systems have reported similar degradation pathways.

For indigo carmine, degradation is initiated by ROS, particularly hydroxyl radicals, interacting with the sulfonate-containing dye molecules. During oxidation, sulfate-containing intermediates may form before complete mineralization. These observations emphasize the importance of photogenerated holes, which participate indirectly by producing hydroxyl radicals through the reactions described in Eqs. (7) and (8). The sulfonate groups increase indigo carmine's susceptibility to oxidative attack, facilitating photocatalytic decomposition under ultraviolet irradiation.

3.3 Recyclability Test

Fig. 11 presents the recyclability and stability of the synthesized photocatalysts, namely (CuO)c, (CuO)gs, (TiO_2)c, and (TiO_2)gs, during degradation of Congo red dye and indigo carmine over five consecutive reaction cycles. Degradation efficiencies decreased only from 55% to 49% for (CuO)c, 71% to 65% for (CuO)gs, 93% to 88% for (TiO_2)c, and 82% to 75% for (TiO_2)gs between the first and fifth cycles. These results demonstrate good photocatalytic stability and reusability of the synthesized nanomaterials, indicating their suitability for repeated wastewater treatment applications. According to previous studies, the CuO/TiO_2 photocatalyst retained its activity with only about 2% efficiency loss after four reuse cycles, confirming the durability of this composite system for repeated dye degradation (Nazari *et al.* 2024).

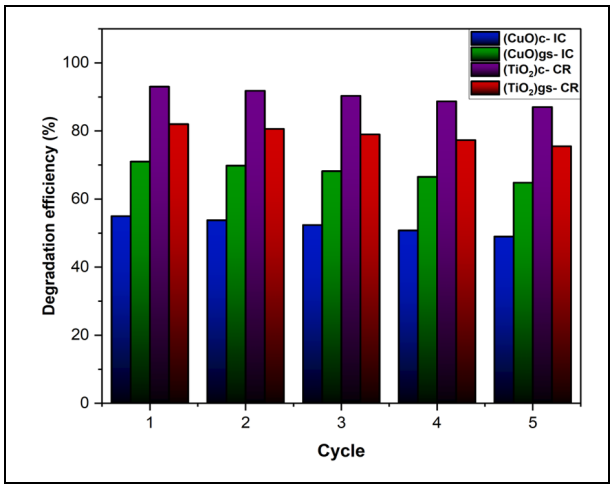

Fig. 11: Reusability efficiency of synthesized nanoparticles over repeated photocatalytic degradation cycles

This approach shows that efficient photocatalytic degradation can be achieved using a low-power UV source and a simple, cost-effective sol–gel synthesis route, without complex mixed-metal oxide

systems, heterostructure engineering, or carbon-based support materials. The synthesized titanium-based oxide NPs exhibited excellent photocatalytic activity and stability, highlighting the effectiveness of the developed green fabrication strategy for sustainable wastewater treatment applications.

4. CONCLUSION

Copper- and titanium-based oxide nanoparticles were successfully synthesized through conventional and bio-assisted sol–gel methods, yielding (CuO)c, (TiO_2)c, (CuO)gs, and (TiO_2)gs. Pomegranate peel extract served as a natural reducing and stabilizing agent during green synthesis. XRD and FT-IR analyses confirmed the formation of crystalline metal–oxide structures with no significant changes in lattice parameters. Green synthesis increased the surface hydroxyl groups in the copper-based oxide and modified the optical properties of both materials. The band-gap energy increased from 1.89 to 2.58 eV for the copper-based oxide, while it decreased from 3.02 to 2.82 eV for the titanium-based oxide. Photoluminescence results indicated band-to-band recombination in copper-based oxides and defect-assisted recombination in titanium-based oxides.

Under UV irradiation for 180 min, (CuO)gs achieved 69% degradation of indigo carmine, compared with 55% for (CuO)c. Its enhanced activity was associated with higher surface hydroxyl concentration, more favorable zeta potential, increased band-gap energy, and improved charge-transfer behavior. Superoxide radicals were identified as the primary reactive species. For Congo red, (TiO_2)c and (TiO_2)gs achieved degradation efficiencies of 93% and 82%, respectively. Hydroxyl and superoxide radicals played dominant roles, while photogenerated holes contributed less significantly. These differences in photocatalytic performance were attributed to variations in dye structure, adsorption behavior, surface charge, and charge-carrier dynamics. Importantly, all photocatalysts maintained nearly constant activity over five reuse cycles, demonstrating their stability, durability, and potential for reusable photocatalytic treatment of dye-contaminated wastewater.

FUNDING

This research received no specific grant from any funding agency in the public, commercial, or not-for-profit sectors.

CONFLICTS OF INTEREST

The authors declare that there is no conflict of interest.

COPYRIGHT

This article is an open-access article distributed under the terms and conditions of the Creative Commons Attribution (CC BY) license (http://creativecommons.org/licenses/by/4.0/).

REFERENCES

Alanazi, A. A., Elattar, K. M., Abdulaziz, F. and Hammouda, M. M., Green fabrication of CuO-Fe_2O_3 and CuO-Fe_2O_3@Chitin nanocomposites using rosemary extract: Structural, antioxidant, antibacterial, and catalytic Indigo Carmine dye degradation performance, *Int. J. Bio. Macromol.*, 352, 151032(2026). https://doi.org/10.1016/j.ijbiomac.2026.151032

Al-Maliki, R. M., Khazal, S. B. and Al Hinai, A., A Review of Historical Nanoscience, Low-Dimensional Nanomaterials: The Art of Fabrication, Characteristics, and Applications in Wastewater, *J. Water Environ. Nanotechnol.*, 11(1), 104–143 (2026). https://doi.org/10.22090/jwent.2026.01.09

Arulnangai, R., Ganesamoorthy, R., Mohamed, V. B. H., Vivekanand, P. A., Kavitha, P., Kavitha, P. and Thirugnanasambandham, K., Green synthesis of silver nanoparticles from Centella asiatica and its application in photodegradation of methylene blue dye in paper industry effluent, *Cleaner Water*, 4, 100179 (2025). https://doi.org/10.1016/j.clwat.2025.100179

Azizi, A., Shariati, M., Hatamipour, S., Khaghaninejad, S. and Ghorbanpour, M., Green synthesis, characterization, and photocatalytic activity of magnetic tin oxide nanocomposites: a case study of modeling and optimization of Rhodamine B degradation with RSM, *3 Biotech.*, 15(12), 433(2025). https://doi.org/10.1007/s13205-025-04616-8

Baran, A. E., Ateş, S. and Sığırcık, G., CuO-TiO_2 nanostructures prepared by chemical and electrochemical methods as photo electrode for hydrogen production, *Int. J. Hydrogen Energy*, 47(10), 6519–6534(2022). https://doi.org/10.1016/j.ijhydene.2021.12.032

Basavarajappa, P. S., Seethya, B. N. H., Ganganagappa, N., Eshwaraswamy, K. B. and Kakarla, R. R., Enhanced Photocatalytic Activity and Biosensing of Gadolinium Substituted $BiFeO_3$ Nanoparticles, *Chem. Select*, 3(31), 9025–9033 (2018). https://doi.org/10.1002/slct.201801198

Ben, M. F., Meskher, H., Menaa, S., Bencheikh, F., Zohra Nouasria, F., Henni, A., Achi, F. and Belkhalfa, H., Dual green reduction mechanisms to prepare rGO-CoNPs nanocomposite using pomegranate peel extract: Electrochemical and photocatalysis applications, *Chem. Phy. Lett.*, 851, 141490(2024). https://doi.org/10.1016/j.cplett.2024.141490

Bopape, D. A., Mathobela, S., Matinise, N., Motaung, D. E. and Hintsho-Mbita, N. C., Green Synthesis of CuO-TiO_2 Nanoparticles for the Degradation of Organic Pollutants: Physical, Optical and Electrochemical Properties, *Catal.*, 13(1), 163(2023). https://doi.org/10.3390/catal13010163

Boudraa, R., Talantikite-Touati, D., Souici, A., Djermoune, A., Saidani, A., Fendi, K., Amrane, A., Bollinger, J. C., Tran, H. N. and Mouni, L., Breaking new grounds: Solid-state synthesis of TiO_2–La_2O_3–CuO nanocomposites for degrading brilliant green dye under visible light, *J. Clean. Prod.*, 481, 144126 (2024). https://doi.org/10.1016/j.jclepro.2024.144126

Bouteiba, A., Benhadria, N., Elaziouti, A., Ezziane, K. and Bettahar, N., Competitive adsorption removal of indigo carmine and congo red dyes from residual effluents by zn2 al-ldh prepared by co-precipitation, *Desalin. Water Treatment*, 201, 404–419(2020). https://doi.org/10.5004/dwt.2020.26016

Deganello, F., Dell'Edera, M., Liotta, L. F., Comparelli, R. and Curri, M. L., Soft-hard templating solution combustion synthesized CeO_2-CuO-TiO_2 nanostructures for visible light photocatalysis, *Catal. Today*, 448, 115169(2025). https://doi.org/10.1016/j.cattod.2024.115169

Djafarou, R., Brahmia, O., Benchikha, N., Dokan, F. K., Sahmetlioglu, E., Atoki, A. V and Messaoudi, M., Dual-Functional and Low-Toxicity ZnO Nanoparticles from Pomegranate Peel: Impact of Synthesis Parameters on Photocatalytic and Supercapacitive Performance, *Chem. Open*, 15(5), e70209 (2026). https://doi.org/10.1002/open.70209

Gaddala, B., Devi, K. V, Balakrishnan, V., Sundramurthy, V. P., Hariprabhu, M., Mayakannan, S., Kadaikunnan, S. and Khaled, J. M., Evaluation of detoxification performance of Pithecellobium dulce seed pod powder upon acid treatment: removal of reactive red 195-A dye and kinetic analysis, *Zeitschrift Fur Physikalische Chemie*, 239(6), 885–910(2025). https://doi.org/10.1515/zpch-2024-0879

Gupta, S., Narayan, H. and Jain, R. K., A review of some metal-oxide based nanocomposites for photocatalytic treatment of wastewater, *Adv. Nat. Sci. Nanosci. Nanotechnol.*, 14(4), 043003(2023). https://doi.org/10.1088/2043-6262/ad002b

Iranfar, S., Hekmati, M., Ziyadi, H., Ghasemi, E. and Esmaeili, D., Synthesis of nanocomposite iron Oxide modified with Punica granatum peel extract and its application in azo dye degradation, *Inorg. Chem. Commun.*, 133, 108925(2021). https://doi.org/10.1016/j.inoche.2021.108925

Joshi, S. J., Geetha, S. J., Al-Mamari, S. and Al-Azkawi, A., Green synthesis of silver nanoparticles using pomegranate peel extracts and its application in photocatalytic degradation of methylene blue, *Jundishapur J. Nat. Pharma. Prod.*, 13(3), (2018). https://doi.org/10.5812/jjnpp.67846

Kozlovskiy, A. L. and Zdorovets, M. V., Study of the photocatalytic activity of irradiated WO_3 microparticles, *Appl. Phy. A: Mater. Sci. Proce.*, 126(8), 638(2020). https://doi.org/10.1007/s00339-020-03827-5

Kumar, A., Poornima, S. N., Subbulakshmi, R., Selvaraju, M., G, R. K. and Jayabalan, C., Hierarchical green carbon fibers from banana pseudostem for efficient Pb^{2+} adsorption: Kinetics, isotherms, and machine learning prediction, *Interact.*, 247(1), 188(2026). https://doi.org/10.1007/s10751-026-02534-6

Leishangthem, N., Das, J., Singh, N. R. and Singh, N. M., Multifunctional metal oxide photocatalysts for water purification: Advances in organic pollutant degradation and antibacterial applications, *Sustainable Chem. One World*, 8, 100128(2025). https://doi.org/10.1016/j.scowo.2025.100128

Mallah, S., El Mchaouri, M., El Meziani, S., Agnaou, H., El Haddaj, H., Boumya, W., Barka, N. and Elhalil, A., Green Photocatalysis: A Comprehensive Review of Plant-Based Materials for Sustainable Water Purification, *React.*, 6(4), 55(2025). https://doi.org/10.3390/reactions6040055

Mancuso, A., Gottuso, A., Parrino, F., Picca, R. A., Venditto, V., Sacco, O. and Vaiano, V., Tuning the selectivity of visible light-driven hydroxylation of benzene to phenol by using Cu, Fe and V oxides supported on N-doped TiO_2, *Green Chem.*, 25(24), 10664–10677 (2023). https://doi.org/10.1039/d3gc02028b

Mehata, M. S., Green route synthesis of silver nanoparticles using plants/ginger extracts with enhanced surface plasmon resonance and degradation of textile dye, *Mater. Sci. Eng. B*, 273, 115418(2021). https://doi.org/10.1016/j.mseb.2021.115418

Meli, A. D., Abdellatief, M., Jamaludin, N. S. and Abdullah, C. A. C., Sustainable Eco-Synthesis of CuO–TiO_2 Nanocomposites Using Hibiscus for Water Remediation, *J. Water Environ. Nanotechnol.*, 10(4), 339–360 (2025). https://doi.org/10.22090/jwent.2025.04.001

Nagajyothi, P. C., Prabhakar Vattikuti, S. V, Devarayapalli, K. C., Yoo, K., Shim, J. and Sreekanth, T. V. M., Green synthesis: Photocatalytic degradation of textile dyes using metal and metal oxide nanoparticles-latest trends and advancements, *Critical Rev. Environ. Sci. Technol.*, 50(24), 2617–2723 (2020). https://doi.org/10.1080/10643389.2019.1705103

Nassar, A. A., Elfiky, A. A. E. A., El-Sawaf, A. K. and Mubarak, M. F., Sustainable green synthesis and characterization of nanocomposites for synergistic photocatalytic degradation of Reactive Orange 16 in textile wastewater using CuO@A-TiO_2/Ro-TiO_2, *Sci. Rep.*, 14(1), 16188(2024). https://doi.org/10.1038/s41598-024-63294-3

Nazari, P., Sohrabi, S., Akhlaghian, F., Mansouri, M. and Mohammadi, M. M. M., Activity, stability, and kinetic study of CuO/TiO_2 Janus photocatalyst for rhodamine B degradation, *Water Practice Technol.*, 19(5), 1893–1907 (2024). https://doi.org/10.2166/wpt.2024.118

Pamitha, P., Veni, K. K., Kavitha, R., Agalya, S., Susanti, D., Sagadevan, S. and Nehru, L. C., Green synthesis of copper oxide and titanium dioxide nanoparticles using Santalum album leaf extract for enhanced wastewater treatment, *Biomass Convers. Biorefine.*, 15(10), 16213–16227 (2025). https://doi.org/10.1007/s13399-024-06332-4

Pamitha, P., Veni, K. K., Kavitha, R., Suresh, S., Wijaya, K. and Nehru, L. C., Enhanced photocatalytic activity of CuO/TiO_2 nanocomposites prepared via chemical and green synthesis for wastewater treatment, *Mater. Chem. Phy.*, 358, 132450(2026). https://doi.org/10.1016/j.matchemphys.2026.132450

Pouthika, K. and Madhumitha, G., Tailoring interfacial charge separation in Z-Scheme CuO@TiO_2@halloysite heterostructure for efficient photocatalytic removal of Congo red, *J. Taiwan Insti. Chem. Eng.*, 166, 105752(2025). https://doi.org/10.1016/j.jtice.2024.105752

Rajesh, Y., Neha, G., Jai, S., Anil, K. T., Gole, S., Pragati, N. and Ganesh, D., Evaluation of Activated Biochar from Sustainable Sterculia foetida Shells for the Removal of AB 158 Dye, *J. Environ. Nanotechnol.*, 13(2), 248-255 (2024). https://doi.org/10.13074/jent.2024.06.242607

Sabzehei, K., Hadavi, S. H., Bajestani, M. G. and Sheibani, S., Comparative evaluation of copper oxide nano-photocatalyst characteristics by formation of composite with TiO_2 and ZnO, *Solid State Sci.*, 107, 106362(2020). https://doi.org/10.1016/j.solidstatesciences.2020.106362

Surendra, V. M., Anburaj, G., Vignesh, C. and Vinoth, K., Green synthesis and multifunctional performance of Cu/TiO_2 nanoparticles from Beta vulgaris leaf extract for diclofenac degradation and biomedical applications, *Spectros. Lett.*, 1-15(2025). https://doi.org/10.1080/00387010.2025.2588443

Wang, R., Cao, J., Liu, J. and Zhang, Y., Synthesis of CuO@TiO_2 nanocomposite and its photocatalytic and electrochemical properties. Application for treatment of azo dyes in industrial wastewater, *Int. J. Electrochem. Sci.*, 18(12), 100316(2023). https://doi.org/10.1016/J.IJOES.2023.100316

Wen, M., Ren, B., Ye, X., He, J., Jiang, H. and Xiong, C., Hierarchical loading of CuO on SiO_2 aerogel@high crystalline TiO_2 nanofibers for efficiently photocatalytic reduction of CO_2 without sacrificial agent, *Nano Res.*, 15(5), 3872–3879(2022). https://doi.org/10.1007/s12274-021-3994-7